A synthetic biology approach defines mechanistic and regulatory roles for phase condensation in the assembly of microtubule architectures by human TPPP

Chih-Chia Chang[1] & Scott M. Coyle[1,2]

Affiliations:
[1] Biophysics Graduate Program
[2] Department of Biochemistry

University of Wisconsin-Madison, Madison, WI, 53705, USA
*Correspondence to: smcoyle@wisc.edu

Summary

Protein condensation regulates numerous cellular processes, but how it participates in the organization of microtubule architectures is unclear. Using synthetic biology approaches to manipulate human Tubulin polymerization-promoting protein (TPPP), we find a microtubule-binding domain and phase-separation motif are sufficient for higher-order microtubule bundling. *In vitro*, native or engineered TPPP phase transitions create multivalent structures that bind and bridge microtubules together. In cells, synthetic modulation of TPPP condensation regulates the strength and lifetime of its microtubule interaction. Surprisingly, cell-scale microtubule assemblies develop when TPPP is connected to synthetic droplets derived from unrelated sequences, mimicking its native localization at Golgi outposts. Systematically targeting TPPP variants to droplet hubs with different biophysical properties defines a two-level scheme for TPPP-regulated microtubule assembly operating at both the nanoscale (microtubule-binding affinity) and microscale (droplet strength). We suggest protein condensates can serve as general-purpose regulatable multivalent bridges for biophysically organizing or engineering microtubule architectures across cellular length-scales.

Introduction

Microtubules (MTs) are one of the major filament systems of the eukaryotic cytoskeleton, extending throughout the cell to build up internal structure, position organelles at specific locations, and facilitate vesicle transport. Individual MT filaments can be further organized into higher-order structures and machines critical for cellular processes, such as the mitotic spindle or ciliary axonemes[1–4]. Such structures depend on the coordinated action of microtubule-associated proteins (MAPs) to organize microtubules in a precise spatiotemporal manner[5,6]. Because microtubules (MTs) are the largest filaments of the eukaryotic cytoskeleton, with a diameter of 25 nm and more than 1600 tubulin subunits per micron[7–9], how the nanoscale actions of MAPs can be effectively integrated across the microscale to build different microtubule architectures is a fundamental question in cell biology.

Protein condensation mediated by liquid-liquid phase separation (LLPS) has emerged as a mechanism for locally concentrating components to drive biochemical interactions and chemistry in cells[10–14]. Although these droplet structures bear little resemblance to the highly ordered structures of the cytoskeleton described above, recent studies have suggested roles for phase separation in amplifying the activity of large MAPs associated with bundling, branching, and tip growth such as tau, TPX2, NuMA, and +TIPs[14–19]. These observations are intriguing, as the high concentrations and reduced-order of liquid condensates in principle could provide both the valency and flexibility needed to couple interacting microtubules across a range of geometries. However, direct evidence for this interpretation is complicated by the fact that these MAPs (1) normally contain multiple MT-binding regions[20–22], (2) may need extra molecular crowders or cytoplasmic extracts to drive their microtubule-directed activity[15,16,23], and (3) often recruit other client proteins to further coordinate MT-crosslinking[17,24,25]. As a result, the specific mechanisms and biophysical principles by which protein condensates directly contribute to the emergent microtubule architectures these MAPs produce is often unclear and their functional relevance and regulation *in vivo* remains elusive.

A MAP with a less complex domain architecture could provide a starting point to directly explore roles for condensation in higher-order MT assembly from the bottom-up using synthetic biology approaches. Tubulin polymerization-promoting protein (TPPP) is a small 24 kDa MAP that contains only a single folded “CORE” domain **(Fig. 1a)**[26,27]. Despite its small size, TPPP is proposed to nucleate and stabilize MTs at discrete structures called Golgi outposts to promote elongation, branching, and polarization of myelin sheaths in oligodendrocytes[28]. TPPP is also involved in aster organization and spindle orientation during early mitosis[29]. Pathologically, TPPP aggregates are associated with Parkinson’s disease and Multiple System Atrophy, and reversing TPPP aggregation has been proposed as a therapeutic strategy[30–32]. Interestingly, the structured domain of TPPP is flanked by low-

complexity intrinsically disordered sequences (IDRs), suggesting a possible role for phase separation in its activity.

Here we use TPPP as a model system for applying synthetic biology approaches to define direct roles for protein condensation in the regulated assembly of microtubule architectures. We show that the structured CORE of TPPP can weakly bind MTs *in vitro*, but bundle-formation requires the presence of its flanking IDRs which allow for TPPP droplet formation. This combination of a MTBD with an IDR is sufficient for activity, as TPPP-CORE MT bundling can be synthetically rescued to near wildtype levels by fusion with condensate-forming IDRs from completely unrelated proteins. To explore how this mechanism can regulate TPPP's biological activity, we reconstituted a synthetically regulated TPPP condensation system in 3T3 cells. Using this tool, we show that the C-terminal IDR of TPPP is critical for its native droplet-regulated interaction with MTs in cells. Surprisingly, MT-bundling and aster formation could be potently induced by targeting TPPP to synthetic droplet-hubs that mimic its native localization at Golgi outposts in oligodendrocytes. By systematically measuring the bundling activity of a range of TPPP variants targeted to synthetic hubs derived from different IDR sequences, we found that TPPP MT bundling activity scales with MT binding affinity and the potency of the IDR. Taken together, this suggests that TPPP activity can be spatiotemporally regulated and tuned by modulating either valency (through condensation) or affinity (targeting the strength of MTBD). Our work provides a new perspective on how cooperation between microscale liquid droplets and nanoscale binding activities can provide a toehold for the regulated assembly of complex MT architectures across cellular length scales.

Results

TPPP's intrinsically disordered regions are necessary for phase-separation *in vitro* and are correlated with its microtubule binding and bundling activity.

Inspection of TPPP's amino acid sequence and AlphaFold structure prediction suggested that TPPP contains a structured "CORE" domain flanked by unstructured N- and C-terminal regions (IDRs), which are common features of phase separating proteins **(Fig. 1a).** To determine if these IDRs allow TPPP to undergo phase separation and whether this correlates with its biological activity, we applied three *in vitro* assays in parallel: 1) a droplet formation assay to determine whether a TPPP construct could phase separate in the presence of crowding reagents; 2) a TIRF-based assay for measuring direct binding to immobilized single MTs in the absence of crowders; and 3) a TIRF-based bundling assay that measures the fraction of microtubules in bundles as a function of TPPP concentration to define an EC50 for quantitative comparison **(detailed in methods).**

We first expressed and purified GFP-tagged full-length TPPP and the isolated TPPP-CORE domain (aa.45-166)—which completely lacks the unstructured N and C termini—and tested each construct for droplet formation. We found that TPPP-FL phase-separated to form drops under a wide-range of different molecular crowding conditions **(Fig. 1b).** In FRAP experiments**,** TPPP-FL droplets showed clear fluorescent recovery over time, suggesting liquid-like properties **(Supplementary Fig. 3a,b and Supplementary Video S1)**. In contrast, no droplets were observed for TPPP-CORE under any conditions tested. Nearly identical results were observed using untagged constructs and DIC microscopy to visualize these droplets **(Fig. 1b and Supplementary Fig. 1a)**. TPPP thus forms protein droplets *in vitro* that depend on the presence of its flanking IDRs.

We then tested if TPPP droplet formation correlated with microtubule binding or bundling activity, measured in the absence of any molecular crowders. Droplet-competent TPPP-FL strongly decorated single-MTs immobilized on coverslips at concentrations as low as 600 nM, while the isolated CORE domain showed weak binding along MTs only at concentrations greater than 6 μM **(Fig. 1c,d and Supplementary Fig 2a,b).** Similarly, while TPPP-FL showed strong MT bundling activity (EC_{50}=0.54 μM), TPPP-CORE bundling was barely detectable even at concentrations greater than 6 μM **(Fig. 1d)**. Thus, TPPP's *in vitro* MT binding and bundling activity is correlated with its ability to form droplets.

To further characterize the relationship between droplet formation and TPPP activity, we applied these assays to a series of TPPP truncations. Neither the N-terminal IDR (aa.1-44) nor the C-terminal IDR (aa.167-219) sequences were sufficient on their own to form droplets, bind, or bundle MTs **(Fig. 1e,f and Supplementary Fig 1b,c,2b).** However, when fused to the TPPP-CORE domain, both the N-terminal IDR (TPPP N-CORE) or the C-terminal IDR (TPPP C-CORE) could support droplet formation, MT binding, and MT bundling. This suggests cooperation between the structured CORE and IDR sequences in droplet formation and TPPP activity (**Fig. 1e-g and Supplementary Fig 2b)**. Fine-scale truncations of the N-terminal IDR and C-terminal IDRs in this context showed that droplet size scaled with the length of the IDR extension **(Fig. 1f)**. Importantly, a TPPP variant's quantitative droplet forming activity correlated with its performance in our MT-bundling and single-MT binding assays (**Fig. 1e-g and Supplementary Fig 2b)**. These data suggest that not only is TPPP droplet formation critical for activity, but that the magnitude of droplet formation can directly control and tune its microtubule bundling efficiency.

TPPP activity can be synthetically rescued using alternative phase modules, allowing systematic investigation of the role of droplets in MT bundling.

Our truncation mapping revealed that TPPP requires both its structured CORE domain and its flanking IDRs for microtubule bundling, and that CORE alone can act as a weak MT-binding domain **(Fig. 1e and 2a)**. Thus, one possible role for droplet formation in this system would be to create a high-valency structure that amplifies this weak MT binding activity. However, truncation mapping cannot rule out other biochemical functions for TPPP's native IDRs. To directly test whether droplet formation is *sufficient* to enhance and multimerize the weak binding activity of TPPP-CORE, we designed and characterized synthetic-TPPP variants in which we fused TPPP-CORE to alternative well-characterized phase-separating IDRs with no homology to TPPP: the human IDRs of DDX4 (aa.1-236), FUS (aa.1-214), and LAF-1 RGG (aa.1-200)[33–37]. These synthetic TPPP chimeras provide an orthogonal control knob for directly probing the role of droplet formation in TPPP activity **(Fig. 2a)**.

On their own, the IDRs from DDX4, FUS and LAF-1 were unable to bind or bundle MTs (**Fig. 2c**). However, fusion of these IDRs to the TPPP-CORE domain restored MT binding, bundling and droplet formation activities to differing degrees **(Fig. 2d,e and Supplementary Fig. 2c,d).** We quantified the droplet intensity distributions **(Fig. 2f)** and bundling efficiency **(Fig. 2g)** of these synthetic TPPP chimeras and compared them to native TPPP-FL and truncations. Across synthetic IDR-CORE chimeras, bundling efficiency (EC50) scaled with droplet formation activity *in vitro* (DDX4>FUS>LAF). The strongest of these, DDX4-CORE, had a MT-bundling activity (EC_{50} = 1.47 μM) within 3-fold of wildtype and outperformed many native bundling-competent TPPP-truncations. In contrast, LAF-1 and the phase disruption mutant FUSY27S-CORE[38], which only weakly formed droplets, showed weak MT-bundling activity **(Fig. 2f,g)**. These data indicate that synthetic modulation of TPPP-CORE droplet formation controls and tunes its MT bundling activity analogously to its native IDRs.

While these assays imply that synthetic TPPP-CORE-IDR fusions can stimulate microtubule bundling, they cannot resolve ultrastructural differences between the resulting bundled architectures **(Fig. 2b,d)**. We thus examined the structure of native and synthetic TPPP microtubule bundles by negative stain electron microscopy. As has been reported previously, TPPP-FL bundles microtubules into long arrays of tightly aligned microtubules[27]. In contrast, no bundling was observed for the phase-deficient TPPP-CORE **(Fig. 2b)**. Synthetic IDR-CORE chimeras produced microtubule bundles in EM that agreed with their quantitative behavior in our *in vitro* bundling assays. DDX4-CORE (EC_{50}~ 1.47 μM) produced bundles that closely resembled those seen for TPPP-FL, creating densely packed structures in which multiple microtubules were aligned together **(Fig. 2d)**. The weaker (EC_{50}~ 5.92 μM) FUS-CORE produced more disperse and less tightly-packed microtubule bundles, and we frequently observed large protein clusters at locations that joined multiple microtubules together **(Fig. 2d)**. No bundled structures were seen for LAF-1-CORE, although some protein clusters were detected on the surfaces of single microtubules **(Fig. 2d)**.

Interestingly, although the strongest droplet-forming sequence (DDX4) produced the most potent microtubule bundling when fused to TPPP-CORE, it also showed the least amount of free protein clusters adhered to MTs by EM. We hypothesized that for both native TPPP and synthetic-TPPP chimeras, as highly aligned MT-bundle structures form, the liquid-like properties of free protein droplets could become more ordered or gel-like as specific interactions between TPPP and MTs develop. To test, we used FRAP to compare dynamics of native and synthetic TPPP variants within droplets to within microtubule bundles. TPPP-FL fluorescence recovered more slowly when assembled into microtubule bundles compared to in the free droplet, and this phenomenon was consistently observed across native TPPP variants with strong droplet-forming activity **(Supplementary Fig. 3a,b and 4a,b)**. Similarly, synthetic DDX4-CORE and FUS-CORE constructs (strong droplet formation and MT-bundling activity) also showed a similar reduction in fluorescence recovery in bundles compared to free protein droplets **(Supplementary Fig. 3c,d and 4c,d)**.

Taken together, our synthetic rescue of TPPP-CORE bundling activity using alternative orthogonal IDR sequences demonstrates that the combination of a weak MT binding domain with a phase separation enhancing motif is sufficient to stimulate bundle formation *in vitro*. Moreover, this synthetic approach allowed systematic trends for arbitrary droplet formation activity in controlling MT bundling activity to be identified. The strong correlation we observed between droplet-formation activity and MT bundling across both native and synthetic TPPP variants suggests that regulation of droplet formation could provide a general mechanism for controlling TPPP activity in cellular contexts.

Synthetic reconstitution of TPPP condensation in living cells reveals a critical role for the C-terminal IDR in droplet-regulated MT interaction.

Our *in vitro* results suggest that TPPP activity in living cells could be regulated by controlling when and where it is allowed to condense into droplets. To the relevance of this mechanism, we installed a synthetically regulatable TPPP-condensation system in 3T3 cells to reconstitute TPPP activity from the bottom-up, allowing systematic investigation of the requirements for microtubule interaction and bundling activity **(Fig. 3a)**. To achieve this, we connected different TPPP variants to the "OptoDroplets" system, a technology that has been broadly applied to study droplet formation and phase transitions in cells[39,40]. In this system, blue-light stimulation clusters target proteins together, increasing their local concentration to sufficiently high levels to drive phase separation of IDR-containing proteins in cells. We first validated this tool by expressing either mCh-Cry2WT or FUS-mCh-Cry2WT as a negative and positive control respectively **(Fig. 3b)**. As expected, mCh-Cry2WT showed no clusters upon light stimulation, while FUS-mCh-Cry2WT formed spherical drops distributed throughout the cell[40]**.** Importantly, these controls showed no cross-reactivity of OptoDroplets with the microtubule cytoskeleton as visualized by the live-cell stain SiR-tubulin.

We next applied this tool to study the behavior of TPPP upon light-induced clustering. Prior to blue-light stimulation, droplet-competent TPPP-FL showed a diffuse distribution within the cell with only faint microtubule decoration. However, upon 5 minutes of blue-light stimulation, TPPP FL formed clusters that associated with and decorated the MTs lattice of the cell **(Supplementary Fig. 5a,b and Supplementary Video S2)**. These TPPP clusters were most dense around the exterior of the nucleus where MTs of 3T3 cells most concentrated. In contrast, the droplet-deficient TPPPCORE-mCh-Cry2WT remained diffuse upon blue-light stimulation and no cluster formation was observed **(Fig. 3c and Supplementary Video S4)**. These data suggest that the flanking IDRs of TPPP we found to be critical for droplet-formation *in vitro* are also required for cluster-driven condensation onto MTs in living cells.

To more precisely define the role of TPPP's native IDRs for MT association in cells, we tested the same series of TPPP variants we examined *in vitro* in the OptoDroplets system. We first examined the importance of TPPP's N-terminal IDRs and C-terminal IDRs. TPPP C-CORE performed comparably to TPPP-FL, producing clusters that clearly decorated the MT lattice of the cell **(Fig. 3c and Supplementary Video S3)**. In contrast, TPPP N-CORE showed no light-dependent clustering onto MTs under any conditions we tested **(Supplementary Fig.**

5a). Although N-CORE showed bundling and binding activity *in vitro*, its activity was quantitatively weaker than TPPP-FL and TPPP C-CORE. This suggests that the requirements for TPPP droplet-regulated interaction with MTs in a living cell may be more stringent than in a minimal *in vitro* system. Mapping the behavior of additional TPPP truncations, we observed that the cluster-dependent MT binding became more pronounced the more we extended C-terminal IDR from TPPP-CORE **(Fig. 3d)**. Extending the N-terminal IDRs from this C-terminally extended TPPP context neither disrupted nor improved cluster-dependent MT association. From this analysis, we were able to define a minimal fragment (TPPP 45-196) that retains cluster-dependent MT association **(Fig. 3d)**.

This experimental setup also allowed us to investigate the effects of TPPP's native IDRs on its disassembly dynamics when bound to microtubules, providing a cell-based analog to the FRAP experiments we performed *in vitro*. We stimulated cells with blue light for 5 min to assemble TPPP clusters onto MTs, and then monitored cluster disassembly over time in in the dark. Consistent with previous reports[40], optically induced FUS-mCherry-Cry2 control droplets completely disassembled within 30 minutes in the dark **(Fig. 3e,f)**. In contrast, optically clustered TPPP-FL showed slow disassembly from MTs, with almost half of all TPPP clusters remaining bound after one hour **(Fig. 3e,f)**. This mirrors the slow fluorescence recovery we observed for TPPP *in vitro* when bound to microtubules compared to in droplets **(Supplementary Fig. 3a,b and 4a,b)**. Applying this technique to our panel of TPPP variants, we found TPPP disassembly kinetics scaled inversely with *in vitro* and in cell droplet-formation activity. Notably, TPPP C-CORE showed nearly identical disassembly kinetics as TPPP-FL, providing further evidence that the C-terminal IDR is critical for its native MT-directed activity in cells **(Fig. 3e,f)**.

Collectively, these observations suggest that the droplet-forming activity of TPPP we observe *in vitro* plays a critical role in controlling its association with microtubules. Moreover, we recapitulated in cells the slow exchange behavior of MT-associated TPPP we observed in our *in vitro* FRAP experiments **(Supplementary Fig. 6a,b)**. These results suggest that regulated condensation of TPPP can control its activity and that the strength of condensation can regulate the lifetime of the MT assemblies it generates.

Reconstitution of higher-order MTs architectures in cells by targeting TPPP to synthetic droplets hubs that mimic the Golgi outpost.

Our OptoDroplets experiments revealed that light-induced clustering of native TPPP allows it to associate with MTs in 3T3 cells in a manner that depends on its C-terminal IDR. However, these bottom-up synthetic efforts did not reproduce the large-scale MT bundles observed *in vitro* and in the oligodendrocyte cytoskeleton. We noticed that the number of TPPP clusters generated using the OptoDroplets system was high and potentially too finely dispersed to coalesce into higher-order architectures on the timescales accessible to light-stimulation. By comparison, the native mechanism for controlling TPPP activity in oligodendrocytes is proposed to depend on its targeting to a recently discovered class of discrete and highly localized cell-type specific structures called Golgi outposts **(Fig. 4a**)[28,41–43]. These outposts are thought to act as hubs that concentrate TPPP with interaction partners, including the droplet-forming Golgi matrix protein GM130[42,44,45]. Inspired by this model, we hypothesized that we could synthetically drive TPPP MT bundling in cells by targeting its condensation to engineered droplet hubs that mimic the Golgi outpost structure.

To develop these hubs, we took advantage of previous work showing that PixD/PixE proteins from *Synechocystis* can form persistent, micrometer-sized liquid-like droplets when fused with IDR sequences[46–48]. To turn these pre-formed droplet structures into hubs for recruiting TPPP, we fused one half of the rapamycin-dependent dimerization system FRB to the PixDE-IDR construct and fused the other half FKBP to our panel of TPPP variants. This enabled us to inducibly target TPPP variants to pre-formed droplet hubs derived from different IDR sequences and monitor the resulting effects on the microtubule cytoskeleton **(Fig. 4a)**.

We first examined the effect of targeting TPPP-FL-FKBP to FRB-DDX4-PixDE droplet hubs in 3T3 cells. Prior to addition of rapamycin, TPPP FL-FKBP was distributed throughout

the cytoplasm and weakly decorated MTs at the nuclear periphery **(Fig. 4b,c)**, consistent with our OptoDroplets experiments and previous studies **(Supplementary Fig. 5a)**[31,49]. Strikingly, rapamycin-induced targeting of TPPP-FL-FKBP to FRB-DDX4-PixDE droplet hubs drove rapid assembly and extensive MT bundling within the cell **(Fig. 4b)**. Detailed inspection of this bundling process revealed that droplet hubs were the initial sites of microtubule interaction **(Fig. 4c)**. Droplets began to deform within seconds of TPPP coupling and completely spread across the microtubule surface within 15 minutes. Over twelve hours, interactions between adjacent TPPP-coated microtubules resulted in extensive redistribution of the cell's MT network into a persistent nest-like bundle surrounding the nucleus in which the SiR-tubulin signal increased >3 fold relative to the start of the experiment **(Fig. 4b-d and Supplementary Video S5)**. Remarkably, these large synthetic MT structures were not dead-ends or cytotoxic, as they were disassembled during mitosis and rapidly reassembled in daughter cells following division. Thus, targeting TPPP condensation to a DDX4-droplet hub created a new interphase-specific synthetic microtubule bundled architecture **(Supplementary Video S6)**.

TPPP has also been proposed to play a role in the nucleation of microtubules at Golgi outpost hubs in oligodendrocytes[28,42]. However, in 3T3 cells, microtubule nucleation through the centriole MTOC dominates the cell's interphase MT network. Thus, to test whether sending TPPP to a droplet-hub could stimulate aster formation, we first treated cells with nocodazole to depolymerize all microtubules. We then targeted TPPP to PixDE-DDX4 droplets using rapamycin and performed a wash-out experiment[50]. Prior to wash-out, TPPP and tubulin strongly colocalized with DDX4 droplet hubs, but no microtubules were detected owing to the presence of nocodazole **(Fig. 4e)**. However, upon nocodazole wash-out, MT filaments rapidly emerged from many TPPP droplet-hubs in an aster-like structure **(Fig. 4f and Supplementary Video S7)**. Over time, multiple droplet-asters clustered and fused together to form MT bundles that coalesced into nest-like architectures as described earlier **(Supplementary Fig. 7 and Supplementary Video S7)**. This result suggests that the ability of TPPP droplet-hubs to trigger MT bundling can also stimulate and stabilize the nucleation of new MTs when appropriately isolated from other sources of MT nucleation and polymerization, as might be expected for distal Golgi outpost hubs in oligodendrocytes. Thus, although our synthetic hubs do not directly represent the native mechanism by which TPPP activity is regulated in oligodendrocytes, they show that condensing TPPP at discrete hubs is sufficient to recapitulate much of the phenomenology of the native TPPP-regulated cytoskeleton.

Systematically targeting TPPP variants to different synthetic droplet hubs suggests a two-level regulatory landscape for controlling TPPP activity.

Targeting TPPP-FL to a DDX4 droplet hub led to extensive bundling activity, which could be quantified by tracking accumulation of MTs towards the perinuclear region of the cell over time. These metrics allow us to take a systematic approach to define how bundling activity is quantitatively affected by either 1) the biophysical properties of the IDR-droplet or 2) the underlying activity of the TPPP variant that we target to these hubs.

To compare the effect of different IDR droplet-hubs **(Fig. 5a)**, we first expressed different FRB-IDR-PixDE constructs in 3T3 cells and characterized the size, number, and exchange dynamics of the resulting hubs. We found that FRB-DDX4-PixDE created the greatest number of large droplets (>1000 a.u.) in cells, followed by FRB-FUS-PixDE and FRB-LAF-1-PixDE **(Fig. 5b,c)**. Using FRAP, FRB-DDX4-PixDE droplets showed the fastest recovery rate, while the FRB-FUS-PixDE and FRB-LAF-1-PixDE drops were slower **(Supplementary Fig. 8a,b)**. These results mirror our *in vitro* characterization of these IDR sequences (DDX4>FUS>LAF-1). We then targeted TPPP-FL to each class of IDR droplet-hub and quantified bundle formation at the single-cell level across multiple replicate cells **(Fig. 5d)**. When TPPP-FL was recruited to DDX4 droplet-hubs, MT-bundling was strong, producing the highest density of MTs in bundles over a 10-hour period. FUS droplet-hubs also produced substantial MT bundling, showing a similar rate of bundling as DDX4 but with slightly reduced basal activity and a lower end-point. In contrast, the weaker droplet-forming LAF-1 hubs showed significantly lower bundling rates and lower end-point bundling **(Fig. 5d and**

Supplementary Fig. 9a-h). These trends mirror the timescale for fluorescence recovery of bundles subjected to FRAP in living cells (DDX4>FUS>LAF1), consistent with the transition to a more ordered state we observed in our *in vitro* and OptoDroplets **(Supplementary Fig. 10a,b)**. Thus, our data indicate that the extent of TPPP bundling in the cell can be set by controlling the biophysical properties of the droplet-hub it is targeted to.

Having seen that DDX4 droplet-hubs had the most consistent and striking effects on TPPP bundling, we next tested the ability of different TPPP variants to stimulate MT-bundling activity when targeted to these hubs **(Fig. 5e,f)**. We found that TPPP variants with strong MT-association *in vitro* and in the OptoDroplets assay showed the strongest microtubule bundling activity when targeted to DDX4-droplet hubs (e.g. C-CORE) **(Fig. 5f and Supplementary Fig. 11a-c)**. Variants that could bundle microtubules *in vitro* but showed poor activity in the OptoDroplets assay showed limited activity (e.g. N-CORE) **(Fig. 5f and Supplementary Fig. 11d-f)**. Interestingly, targeting TPPP-CORE to DDX4 droplets drove weak, but detectable, MT bundling in this assay, consistent with our in vitro observations that TPPP-CORE activity could be rescued by alternative IDRs **(Fig. 5f, Supplementary Fig. 11g-l and Supplementary Video S8)**. However, the degree of rescue here is dramatically lower than what we observed *in vitro*. Indeed, the majority of TPPP-CORE remained in droplets when targeted to DDX4 hubs, in contrast to other TPPP variants that induced droplet-spreading along the MT surface. This suggests that although a droplet hub can enhance a weak MT-binding activity, if the droplet-forming activity is too strong it may outcompete the target MT interaction in the context of a living cell.

Having collected experimental bundling activity data from a range of TPPP variants and synthetic droplet hubs across more than a hundred different cells, we mapped these metrics onto a phase space defined by a TPPP variant's MT interaction strength (defined by the extent of MT decoration *in vitro*) and strength of the IDR hub (defined by the frequency of observation of large droplets). Interpolating our data produced a phenomenological picture of the regulatory landscape for TPPP activity **(Fig. 5g)**. At the level of individual TPPP molecules, stronger MT interaction strength allowed for some MT bundling even in the absence of direct targeting to a droplet hub. Bundling activity dramatically increased across all variants when targeted to a strong droplet hub (DDX4), but TPPP variants with reduced MT interaction strength only moderately stimulated bundling activity when targeted. Together, this landscape suggests two routes for spatiotemporal control of TPPP activity in cells: modulation at the protein level, targeting how strongly TPPP can bind to microtubules; or modulation at the microscale, targeting TPPP droplet-formation and condensation **(Fig. 5g,h)**.

Discussion

In this work, we used the small 24 kDa human oligodendrocyte MAP TPPP as a model system for applying synthetic biology approaches to define roles for protein condensation in the assembly of higher-order MT architectures from the bottom-up. Our *in vitro* experiments demonstrated that TPPP MT bundling requires both a structured CORE domain that weakly binds MTs as well as flanking disordered sequences (IDRs) that stimulate formation of TPPP droplets **(Fig. 1b-g and 2a)**. These native IDRs could be functionally replaced by synthetic droplet forming sequences from other unrelated proteins, showing that the combination of MT binding and droplet formation is sufficient for MT bundling activity *in vitro* **(Fig. 2a-g)**. Extending these synthetic biology approaches to cells, we defined how TPPP activity could be regulated by droplet formation by reconstituting TPPP cluster formation and bundling activity exogenously in 3T3 cells. Using the OptoDroplets system, we found that TPPP's C-terminal IDR permitted rapid droplet-mediated interaction of TPPP with the MT cytoskeleton **(Fig. 3c,d and Supplementary Fig 5a,b)**. Moreover, TPPP could drive potent MT bundling and aster formation when targeted to synthetic IDR droplet-hubs that emulate the discrete, localized structure of the native Golgi outpost to which TPPP is targeted in oligodendrocytes **(Fig 4b,f)**. By measuring bundling efficiency as we systematically varied the strength of the TPPP/MT interaction (through different TPPP variants) or the potency of the synthetic droplet hub (through different IDRs), we uncovered a simple two-level regulatory landscape for

spatiotemporal control of TPPP activity that can operate by either targeting TPPP's ability to interact with MTs or its droplet formation **(Fig 5d,f,g,h)**.

A surprising result that emerged from our synthetic approach is that many of TPPPs most critical activities—MT binding, bundling, and aster formation—can be driven and regulated through the action of arbitrary droplet-forming sequences which have not specifically co-evolved with TPPP to perform these functions. Indeed, the ability of TPPP's MT-binding domain to cooperate so effectively with the IDRs of DDX4—an RNA helicase[51,52]—indicates considerable plasticity in the mechanisms by which droplet-formation can contribute to MT organization. We suspect this flexibility in how TPPP activity can be controlled may explain the multitude of other MT structures TPPP isoforms are associated with outside of oligodendrocytes, including the sperm flagellum (TPPP2)[26,53] and protozoan ciliary lattices[54]. More generally, our results suggest that protein condensates may provide a versatile *biophysical* strategy for coordinating the nanoscale interaction between MAPs and MTs across the cellular length scales needed to reliably assemble specific architectures **(Fig. 5h)**.

At the same time, these general-purpose biophysical mechanisms likely only provide the starting point for the more complex, highly-evolved regulatory mechanisms needed to reliably specify and control assembly of specific target architectures. For example, although TPPP activity could be fully rescued *in vitro* by replacing its IDRs with those of DDX4 and FUS, its performance in cells benefitted from including at least some of its native IDR sequence. Indeed, targeting the TPPP-CORE domain alone to DDX4-droplet hubs resulted in most of it becoming sequestered in the droplet as opposed to MTs. We suspect the specific biochemical requirements for effective coupling between nanoscale MAPs and droplet-forming sequences may require a carefully tuned balance that allows condensates to be able to form but also wet their MT substrates[55]. Nevertheless, these droplet-based biophysical mechanisms for microtubule bundling can provide a starting point for more elaborate evolutionary refinement.

Asking what was required to allow TPPP to synthetically reorganize the interphase MT cytoskeleton of 3T3 cells from the bottom-up also provided insights into constraints on the assembly of TPPP-dependent MT architectures that are complementary to efforts to understand TPPP's native regulation in oligodendrocytes. First, while TPPP was able to potently bundle MTs within the cell, the interphase MT network derived from centriolar MTOCs dominated the overall structure and spatial distribution of the emergent structure towards the cell center[56–58]. Second, TPPP activity benefited from being condensed at a small number of discrete locations as opposed to random locations everywhere throughout the cell body. Third, while TPPP could stimulate aster formation in cells, it could only do so when isolated from the existing pool of interphase MTs. These constraints agree with proposed models for how TPPP is natively able to nucleate MTs far from the cell body of oligodendrocytes, where the centriole-driven MT network is sparse and TPPP is targeted into discrete, isolated Golgi outposts to drive assembly of a localized and TPPP-specific MT network. Because such models can be difficult to test directly, a back and forth between traditional mechanistic investigation in native cell types and build-to-understand synthetic approaches provides a powerful combination for elucidating the design principles that underlie the regulated assembly of complex microtubule architectures, providing a deeper ability to understand the origins of complex microtubule architectures seen in nature and a path forward to engineering new microtubule structures of our own design.

Acknowledgments
We thank members of the Coyle Lab, A. Weeks, W. Bement, A. Suzuki, and C. Lim for advice, helpful discussions.

Funding: This work was supported in part by startup funds from the University of Wisconsin-Madison Department of Biochemistry and by a David and Lucille Packard Fellowship for Science and Engineering (SMC).

Author contributions

CCC and SMC designed the project; CCC performed all experiments and interpreted the data for the manuscript under the supervision of SMC; CCC and SMC wrote the manuscript and contributed to the final version.

Methods

Plasmid construction

Homo sapiens TPPP WT gene was synthesized as gBlocks (Integrated DNA Technologies). TPPP truncation mutants were produced using a standard PCR. All TPPP variant then inserted into the pBH4 vector which contains GFP sequence and His-tag at N-terminal region. Homo sapiens DDX4 (residues 1-236), LAF-1 RGG (residues 1-200) and FUS Y27S mutant (residues 1-214) fragments were obtained as gBlocks (Integrated DNA Technologies). Human FUS (residues 1-214) was amplified by PCR using pHR-FUSN-mCh-Cry2WT (addgene #101223). The IDRs fragments were fused with TPPPCORE domain(aa.45-166) into the same pBh4-His-GFP plasmid. For making the OptoTPPP, different TPPP fragment were produced by PCR then cloned into the pHR-mCh-Cry2WT plasmid.

The DNA fragments of FRB, IDRs, FusionRed-PixD and Citrine-PixE were produced by PCR using existing templates (addgene #31181), (Plasmid #111503) and (Plasmid #111505) and subcloned to SFFV vector to generate FRB-IDR-FusionRed-PixD and FRB-IDR-Citrine-PixE. The DNA fragments of TPPP FL and FKBP were produced by PCR using existing templates and (addgene #31184). The tagBFP gene was synthesized as gBlocks (Integrated DNA Technologies). All fragments subcloned to SFFV vector to generate TPPP-tagBFP-FKBP. For making TPPP variants-tagBFP-FKBP constructs, the DNA fragments were generated by PCR using existing templates and then fused into SFFV promoter vector.

Bacterial protein expression and purification

All TPPP variant and TPPP-chimeras constructs were expressed in BL21(DE3). *Escherichia coli* overnight at 16°C after induction with 0.5 mM IPTG. The culture was harvested by centrifugation and lysed according to the following procedure. The cell pellets were resuspended in lysis buffer (50 mM KH2PO4, 50 mM Na2HPO4, 150 mM NaCl, and 2 mM β-mercaptoethanol), disrupted by French press, and centrifuged at 15,000 g at 4 C for 20 min. The supernatant was incubated with Ni resin (Sigma) for 30 min, followed by a prewash with 25 mM imidazole. Proteins were eluted with the buffer containing 250 mM imidazole. Then the samples were further purified by SEC (Superdex 200 16/60) and analyzed by SDS-PAGE. The protein fraction was collected, concentrated, and stored in a buffer consisting of 20 mM Hepes, pH 7.4, 50 mM NaCl, and 3 mM DTT. All proteins were flash frozen and stored at −80 °C. Before use, all proteins were pre-cleared of aggregates via centrifugation at 4 °C.

Single-microtubule binding and microtubule-bundling assays

Microtubules were polymerized from a solution that contained unlabeled, Alexa Fluor 594-labeled and biotin-labeled tubulin in a ratio of 25:1:1 at 37°C in the presence of GMPCPP. Flow chambers were assembled with biotin-PEG-coated coverslips. The chamber was sequentially filled with 0.5 mg/ml α-casein, 0.2 mg/ml NeutrAvidin, and biotinylated microtubules in 1xBRB80, and 20 μM Taxol. Next, GFP-labeled TPPP variants or TPPP-Chimeras were added to the chamber in 1xBRB80 supplemented with 20 μM Taxol, 0.5 mg/ml α-casein, 10% sucrose, 2 mM DTT, 200 μg/ml glucose oxidase, 35 μg/ml catalase, and 4.5 μg/ml glucose. The chamber was then filled with the solution and sealed, then imaged by using TIRF microscopy. The GFP and Fluor 594 intensities were determined using Fiji.

For a microtubule bundling assay, TPPP variants and TPPP chimeras were incubated with Taxol-stabilized, Alexa Fluor 594-labeled and biotin-labeled tubulin microtubules for 5 minutes. Samples were spotted onto biotinylated coverslip. Microtubule bundles were visualized by a TIRF illumination system, and Fluor 594 intensities were determined using Fiji. Single microtubules and the bundled microtubules' fluorescence were measured using a line profile in Fiji. The background value was subtracted from the same line profile at the local region adjacent to the microtubule to give a corrected intensity measurement, and the bundled microtubule probability was defined. For all saturation curves, a concentration series was

performed for each TPPP variant or TPPP-Chimeras. All the curves were fitted to a one-site-binding hyperbola.

Droplet formation assay
GFP-TPPP variants and TPPP-chimeras with 20 μM in buffer (20 mM HEPES, 50 mM NaCl, 3 mM DTT) containing crowding reagents (12% dextran), respectively. Samples (2 μl) were spotted onto glass slides then visualized using Confocal fluoresce microscopy. Images were visualized GFP signal; then measured and quantified using Fiji.

Fluorescence recovery after photobleaching (FRAP) analysis
GFP-TPPP variants and GFP-SynMAPs droplets were FRAP using confocal microscopy (NIKON A1RS) for a total of 5 min. Defined regions were photobleached and monitored the at the 488 nm wavelength fluorescence intensities. GFP-TPPP variants and GFP-SynMAPs-bundled microtubules were photobleached and monitored at the 488 nm for a total of 2 min. For FUS and TPPP variants-mCh-Cry2WT FRAP, the clusters were activated by 488 nm wavelength blue light for 5 min; then, the light-induced clusters in NIH3T3 cells were bleached and monitored by 561 nm for a total of 1.5 min. For IDRs-FusionRed/Citrine-PixDE FRAP, the droplets were photobleached and monitored at the 561 nm wavelength fluorescence intensities in every 10s intervals for a total of 2 min; the TPPP-IDRs-FusionRed/Citrine-PixDE bundled MTs were FRAP and monitored at the 561 nm wavelength fluorescence intensities in every 5 s intervals for a total of 2 min. Recovery fluorescence intensities were recorded for the indicated time then, quantified and normalized by using Fiji.

Negative stain electron microscopy
The GFP-TPPP FL, GFP-TPPPCORE, and GFP-SynMAPs were mixed with unlabeled GMPCPP-stabilized microtubules in the 1xBRB80 buffer for 5 min at room temperature. The mixed samples were diluted with 1xBRB80 to reduce unbundled microtubules in the background, and a 3 μl mixture was spotted on glow-discharged grids (Electron Microscopy Sciences, CF400-Cu), then stained with 2% uranyl acetate. Images were collected at a magnification of 45,000 using 120 kV Talos L120C at UW-Madison Cryo-EM Research Center.

Construction of stable cell lines
Optogenetic Cry2WT expressing constructs and FRB-IDRs-PixDE/TPPP variants-FKBP constructs were transfected with FuGENE (Promega) into HEK293T to produce lentivirus. Viral supernatants were collected 3 d after transfection and passed through a 0.45-mm filter to remove cell debris then incubated with NIH 3T3 cells containing polybrene 8 μg/mL. Viral medium was replaced with normal growth medium 24 hr after infection. After 3 days, cells were sorted on an FACSAria cell sorter (BD Biosciences) based on fluorescent protein expression levels.

Live cell imaging
Cells were plated on 0.17±5 μm 24 well glass bottom plate (Cellvis) and in the FluotoBrite™ DMEM (ThermoFisher A1896701) overnight. All live cell imaging was performed using 60X oil immersion objective (NA 1.4) on a Nikon Ti-Eclipse with a temperature stage at 37°C and supplied with 5% CO2. NIH3T3 cells were imaged using four laser wavelengths (405 nm for tagBFP; 488 nm for Citrine; 561 nm for mCherry or FusionRed; 674 nm for SiR700-Tubulin Kit, #CY-SC014, Cytoskeleton Inc.).

OptoDroplet assay
The OptoTPPP was designed from a previous study. The NIH3T3 cells were transfected with OptoFUS and OptoTPPP variants constructs. Cells were plated on 0.17±5μm 24 well glass bottom plate (Cellvis) and in the FluotoBriteTM DMEM (ThermoFisher A1896701) for imaging. Cluster formation was induced using Nikon Ti-Eclipse digital micromirror device (DMD) in 475

nm wavelength laser light. The clusters and microtubules were imaged using two laser wavelengths (561 nm for mCherry; 647 nm for SiR700-tubulin).

To quantify the cluster ratio in cells containing clusters, total cluster intensity (I_C) was divided by the whole cell's total fluorescence intensity (I_W) adapted from a previous study[59]. The cluster disassembly rate was based on quantifying cluster formation numbers followed by normalized using Fiji. The curves were determined by fitting them to a one-phase decay equation.

Nocodazole treatments

For microtubule depolymerization, nocodazole (30 μM) was added to culture media for 6 hr. Then the NIH3T3 cells were washed with cold in the FluotoBriteTM medium directly at the microscope with temperature stage at 37°C and supplied with 5% CO2. The heated stage slowly raised the temperature. The regrowth microtubule images were captured using Nikon Ti-Eclipse.

Statistical analysis

Statistical analyses were calculated using Prism (version 9.0c). Figure legends detail the n values and error bars for each experiment. Statistical differences for single-MT binding assay (Supplementary Figure 2c,e) and cluster formation assay (Fig. 3d) were determined by Student's two-tailed t-test; *P< 0.05, **P< 0.01, ***P< 0.001 and ****P< 0.0001.

Figures and Figure Legends.

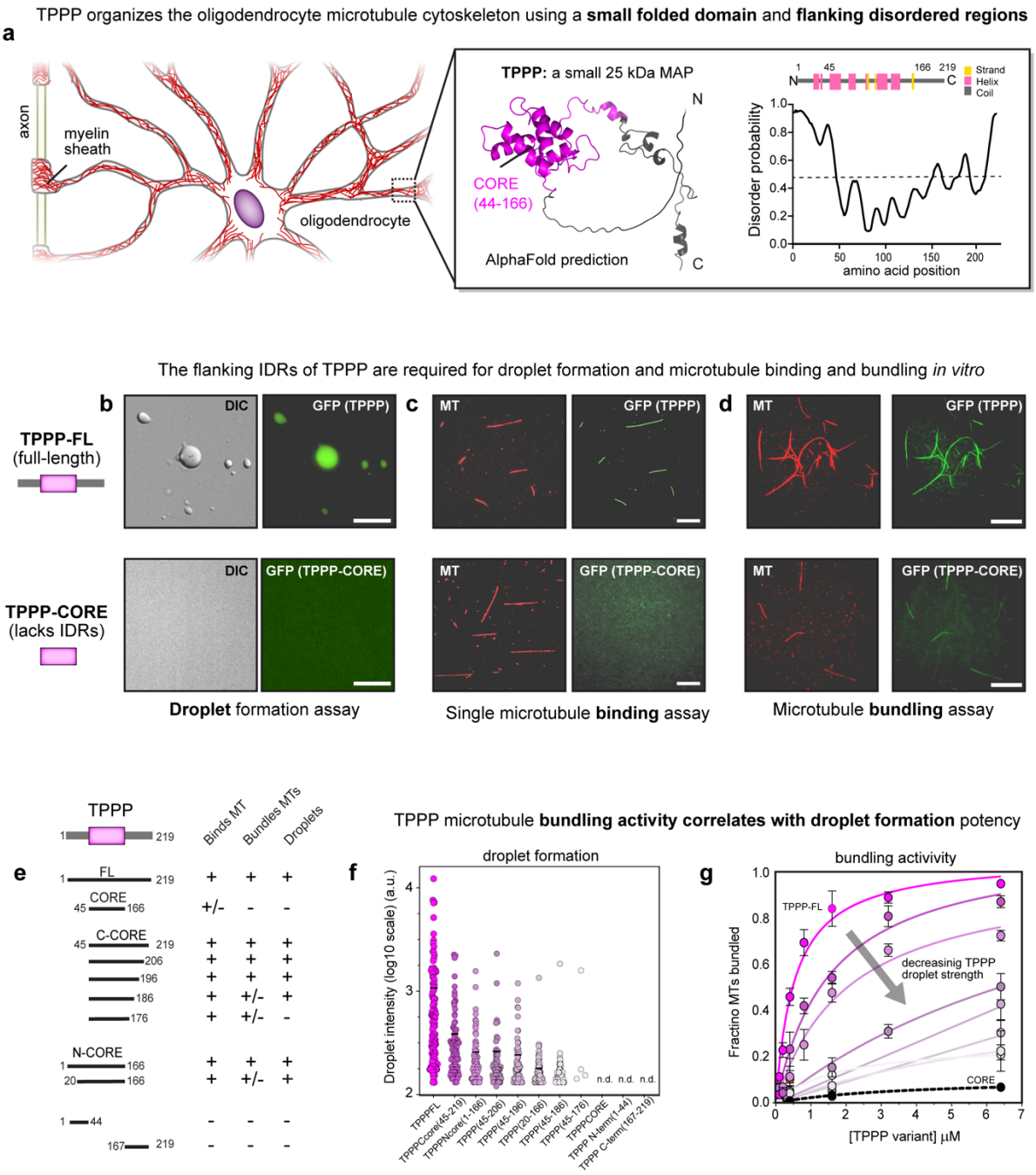

Fig. 1 | **The IDRs of TPPP and its folded CORE domain are necessary for droplet formation, microtubule binding, and bundling activity. a** TPPP is a 24 kDa protein that promotes microtubule nucleation, bundling, and stabilization in oligodendrocytes. A 3D visualization of the AlphaFold structure prediction for TPPP is shown,with the folded CORE domain in pink and unstructured regions in gray. The corresponding secondary structure prediction of TPPP protein domains is indicated, with α-helical and β-strands structures are shown as pink and yellow blocks, along with the PrDOS-predicted intrinsic disorder of TPPP. Higher scores indicate a greater degree of disorder. **b** Epifluorescent image of droplet formation assay. TPPP phase-separated into drops but not the CORE domain in the presence of 12% of dextran crowding agent. DIC (left) and green fluorescence (right) images of GFP-TPPP FL and GFP-TPPP-CORE, both at the concentration of 20 μM with 20 mM HEPES, 50

mM NaCl, 3 mM DTT, and 12% dextran. Bars, 10 μm. **c** TIRF images of single-microtubule binding assay. GMPCPP-stabilized microtubules (Alexa-594 and biotin-labeled) immobilized on a glass surface, were incubated with GFP-TPPP FL and GFP-TPPP-CORE, respectively. Both at the concentration of 600 nM. Bars, 10 μm. **d** TIRF microscopy images of microtubule bundling assay. GFP-TPPP FL and GFP-TPPP-CORE (green) were mixed with in vitro polymerized Alexa-594 (Red), biotin-labeled, and GMPCPP-stabilized microtubules for 5 min, then captured microtubule bundles by NeutrAvidin-coated biotin coverslips. Both at the concentration of 6.4 μM. Bars, 10 μm. **e** Different TPPP variants are assessed for MT-binding, bundling, and droplet formation activities. Symbols denote experiments performed qualitatively. **f** Quantification of GFP-TPPP variants droplets fluorescence signal intensity. The mean was determined from data pooled from five representative images. GFP-TPPP variants droplets number in total five images, respectively; TPPP FL, n = 107; TPPP -Ccore(45-219), n = 92; TPPP-Ncore(1-166), n = 73; TPPP(45-206), n = 53; TPPP(45-196), n = 60; TPPP(20-166), n = 89; TPPP(45-186), n = 90; TPPP(45-176), n = 4. TPPP-CORE(45-166), TPPP N-term, and TPPP C-term showed n.d., not detectable droplets. All GFP-TPPP variants were in the concentration of 20 μM with 20mM HEPES, 50mM NaCl, 3mM DTT, and 12% dextran. **g** MT bundling activity was determined as an EC50 from the fraction of microtubules in bundles as a function of GFP-TPPP variants concentration. TPPP FL, EC50 = 0.54 μM; TPPP-Ccore, EC50 = 1.58 μM; TPPP-Ncore, EC50 = 2.06 μM; TPPP(45-206), EC50 = 10.58 μM; TPPP(45-196), TPPP(45-186), TPPP(20-166), and TPPP-CORE curves and EC50 constants were determined by fitting to a hyperbola. Mean (points) and SEM (error bars) of three replicate experiments (error bars) shown.

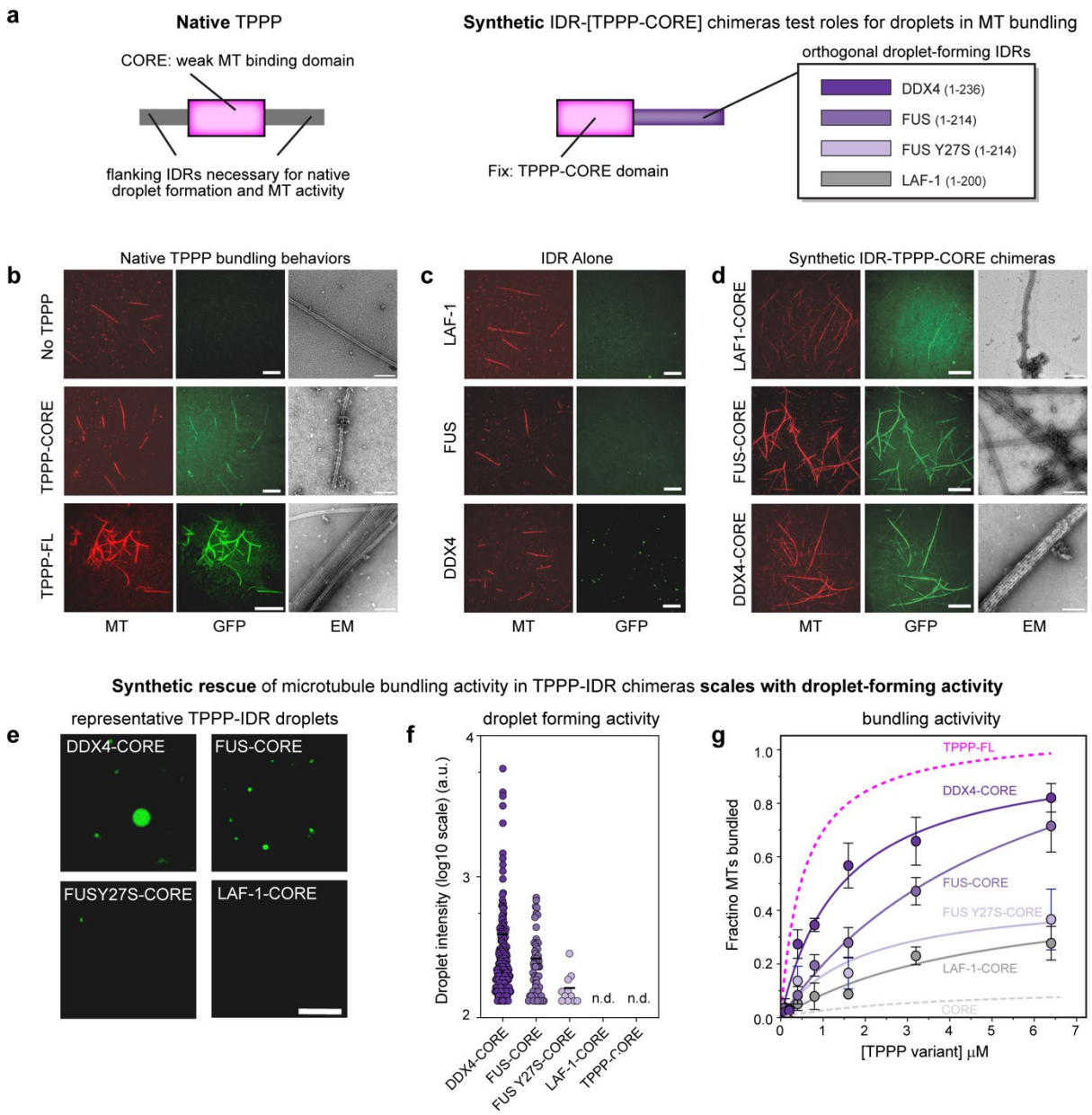

Fig. 2 | **TPPP activity can be synthetically rescued using alternative phase modules, allowing systematic investigation of droplet roles in MT bundling. a** (left) TPPP structured CORE domain can act as a weak MT-binding domain but the bundle formation requires the presence of one of flanking intrinsically disordered regions (IDRs) that drive TPPP droplet formation. (right) Schematic of chimera design: The IDRs of DDX4, FUS, FUSY27S (phase disruption mutant), and LAF-1 were fused with TPPP-CORE domain shown in table. All TPPP-Chimeras were tagged with GFP protein at N-terminal region. **b-d** TIRF and EM images of native TPPP and synthetic MAPs bundling behavior. **b** Microtubule only, TPPP-FL, TPPP-CORE, and control **c** different potent phase-enhancing domains (IDRs of DDX4, FUS, and LAF-1) were tagged with GFP mixed with microtubule spotted on biotin-coverslips in the concentration of 6.4 μM. Bars, 10 μm. **d** The TPPP-Chimeras; GFP-DDX4-CORE, GFP-FUS-CORE, and GFP-LAF-1-CORE were mixed with microtubules and captured by biotin-coverslips in the concentration of 6.4 μM. Bars, 20 μm. For EM images, GMPCPP-stabilized microtubules incubated with TPPP FL, TPPP-CORE, DDX4-CORE, FUS-CORE, and LAF-1-CORE, visualized by electron microscopy after uranyl acetate staining. Bars, 200 nm. **e** Fluorescent image of synthetic MAPs; GFP-DDX4-CORE, GFP-FUS, GFP-FUSY27S-CORE, and LAF-1-CORE droplets *in vitro*. All at the concentration of 20 μM with 20 mM HEPES, 50

mM KCl, 3 mM DTT, and 12% dextran. Bars, 10 µm. **f** Quantification of TPPP-Chimeras droplets fluorescence signal intensity. The mean was determined from data pooled from five different images. SynMAPs-TPPP droplets number in total five images, respectively; DDX4-CORE, n = 179; FUS-CORE, n = 57; FUSY27S-CORE, n = 11; LAF-1-CORE, n = 0; TPPP-CORE, n = 0. All TPPP-Chimeras were tested at the same concentration. **g** MT bundling activity was determined as an EC50 from the fraction of microtubules in bundles as a function of SynMAPs-TPPP concentration. TPPP FL, EC50 = 0.54 µM, data was added for comparison. DDX4-CORE, EC50 = 1.47 µM; FUS-CORE, EC50 = 5.92 µM; FUSY27S-CORE, and LAF-1-CORE curves and EC50 constants were determined by fitting to a hyperbola. Mean (points) and SEM (error bars) of three replicate experiments shown.

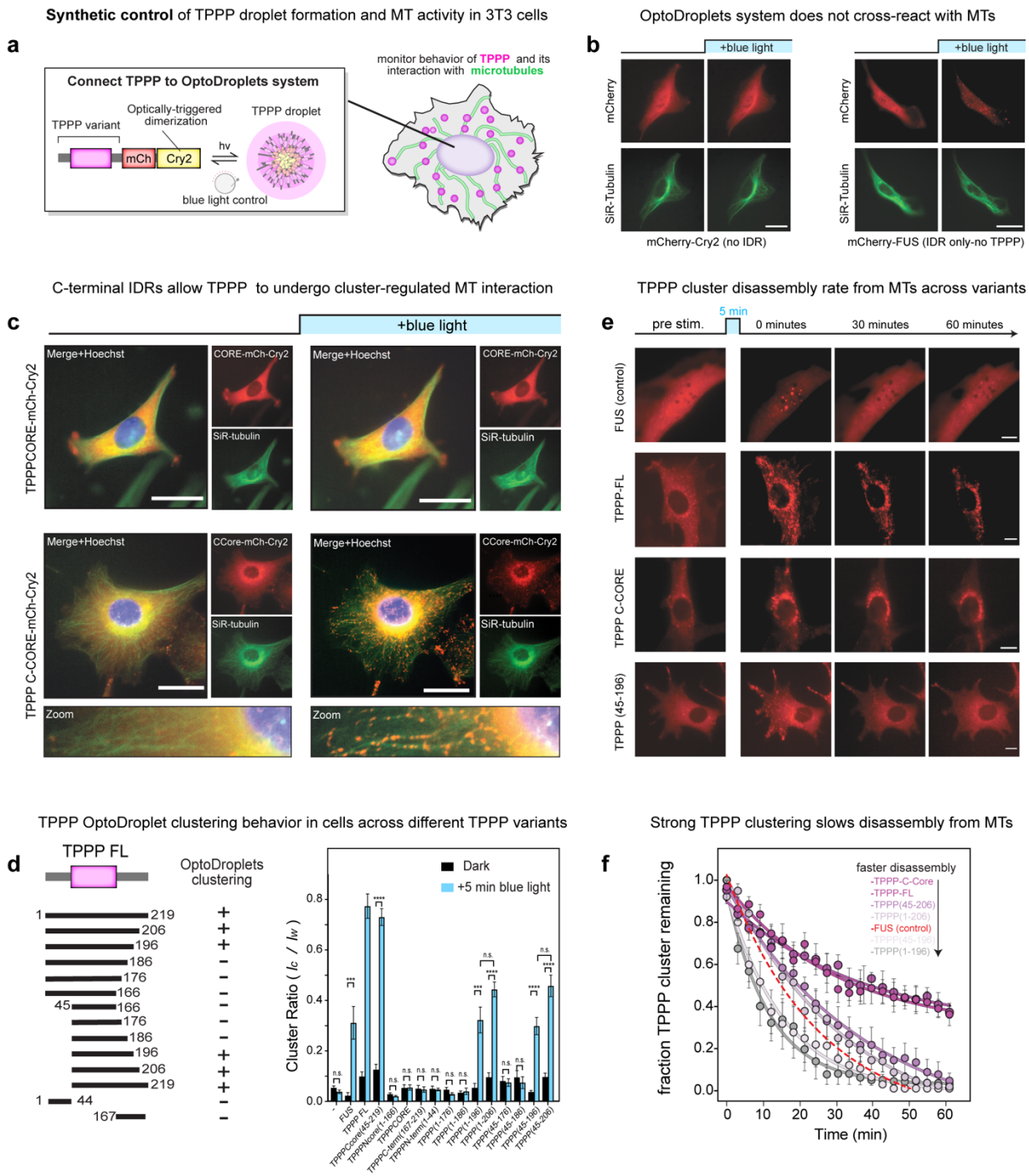

Fig. 3 | **Synthetic reconstitution of TPPP condensation in living cells reveals a critical role for the C-terminal IDR in droplet-regulated MT interaction. a** Schematic diagram of OptoTPPP constructs, in which Cry2WT-mCh is fused to various TPPP fragments to allow blue-light triggered clustering in cells. **b** Representative images pre- and post- 5 min blue light activation for OptoFUS and OptoTPPP in NIH3T3 cells (SiR-tubulin, green; Hoechst, blue). **c** As in b, but for OptoTPPP variants CORE and the C-terminally IDR containing variant C-CORE. Bars, 20 µm. **d** Schematic overview and quantification of the ratio of the OptoTPPP cluster in cells. (left) Summary of OptoTPPP cluster's formation activity upon 5 min blue time stimulation. (right) Quantification of the ratio of the OptoTPPP cluster in cells. Total cluster intensity (I_C) was divided by the total fluorescence (I_W) of the whole cell. Values are expressed as means ± SEM. Cry2WT only, n = 12; FUS, n = 13; TPPP FL, n = 15; TPPPCcore(45-219), n = 15; TPPPNcore(1-166), n = 15; TPPP(1-206), n = 15; TPPP(45-206), n = 15; TPPP(1-

196), n = 12; TPPP(45-196), n = 17; TPPP(1-186), n = 12; TPPP(45-186), n = 14; TPPP(1-176), n = 17; TPPP(45-176), n = 13; TPPPCORE(45-166), n = 12; TPPPN-term(1-44), n = 12; TPPPC-term(167-219), n = 12. Two-tailed Student t test; statistical differences: ****, P < 0.0001; *** P < 0.001; n.s., not significant. **e** Representative images of OptoFUS and OptoTPPP cells under cluster disassembly assay. Blue box indicated as blue light activation for 5 min and then incubated in the absence of blue light for 60 min. Cell images are captured during (pre-activation, after light stimulation; 0s, 30 min and 60 min). Scale bar, 10 μm. **f** Normalized number of Opto-FUS and Opto-TPPP clusters **e** during disassembly in NTH3T3 cells. Values are expressed as means ± SEM. FUS, n = 6; TPPP FL, n = 6; TPPPCcore(45-219), n = 7; TPPP(1-206), n = 7 ; TPPP(45-206), n = 7; TPPP(1-196), n = 6; TPPP(45-196), n = 6. The curves were determined by fitting to a one-phase decay equation.

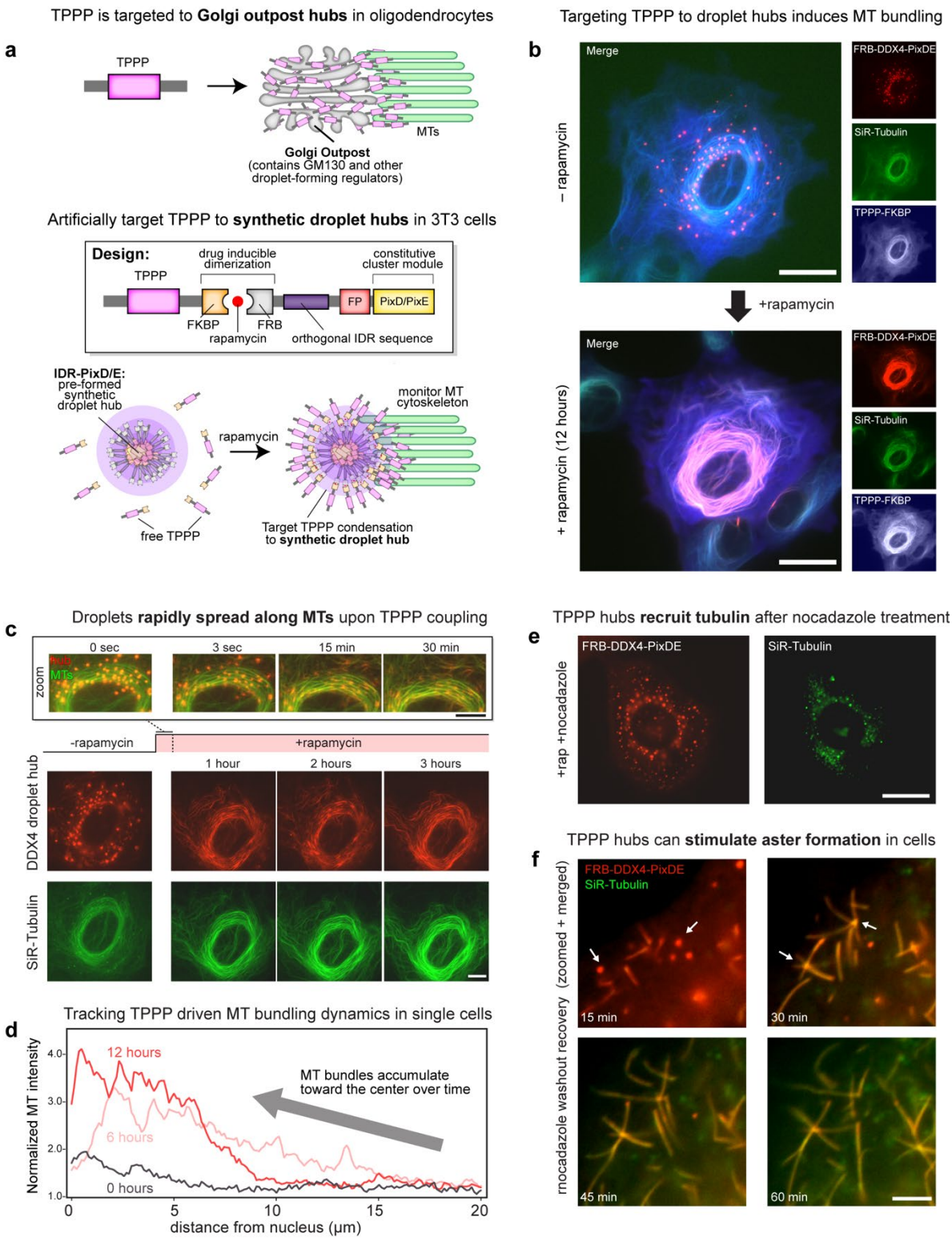

Fig. 4 | **Reconstitution of higher-order MTs architectures in cells by targeting TPPP to synthetic droplets hubs that mimic the Golgi outpost. a** Schematic of the constructs used for inducibly recruiting TPPP into IDRs-droplet hubs, mimicking the discrete and localized native targeting of TPPP to Golgi outposts in oligodendrocytes. The system is based on the rapamycin-inducible dimerization system FKBP/FRB. FRB-IDRs are fused with PixD/E containing fluorescent protein (FusionRed and Citrine) to produce constitutive droplets, and FKBP is fused with TPPP tagged with tagBFP. Upon rapamycin treatment, TPPP will be delivered to the engineered IDRs-droplet hub. **b** Representative images of NIH3T3 cells co-

transduced with FRB-DDX4-PixDE and TPPP FL-FKBP before and after (12 hr) rapamycin treatment. The addition of rapamycin (20 μM) rapidly translocated TPPP (tagBFP, white color in image) into DDX4 liquid droplets (FusionRed, red) and increased bundled microtubules (SiR-tubulin, green). Scale bar, 20 μm. **c** Representative images of a time series of rapamycin-induced TPPP conjugated with DDX4-PixDE drops (Red). Microtubule lattices were stained with SiR-tubulin (green). Zoom view (upper) shows the time series of 0-30 min after rapamycin induction. Scale bar, 10 μm. And representative images (bottom) of 0-3 hr after rapamycin induction. Scale bar, 10 μm. (see also Supplementary Video S5). **d** Quantification of the microtubule fluorescence signal (SiR-tubulin) before and after 6, 12 hours rapamycin treatment distribution in NIH3T3 cells co-transduced with FRB-DDX4-PixDE and TPPP FL-FKBP. Distance from the center of the Nucleus is shown on the horizontal axis, and normalized fluorescence intensity is on the vertical axis. **e,f** TPPP-DDX4 droplet hubs nucleate microtubule. **e** Representative image showing tubulin colocalization with TPPP-droplet hubs in cells treated with nocodazole (30 μM) for six hours. The DDX4-PixDE (FusionRed, red) show the co-localized with tubulins (SiR-tubulin, green) after microtubule disassembly. Scale bar, 20 μm. **f** Live-cell images of nocodazole washout. Video frames (15-60 min) illustrating microtubule aster formation (arrows) originating from TPPP-DDX4 droplet hubs, Scale bar, 5 μm.

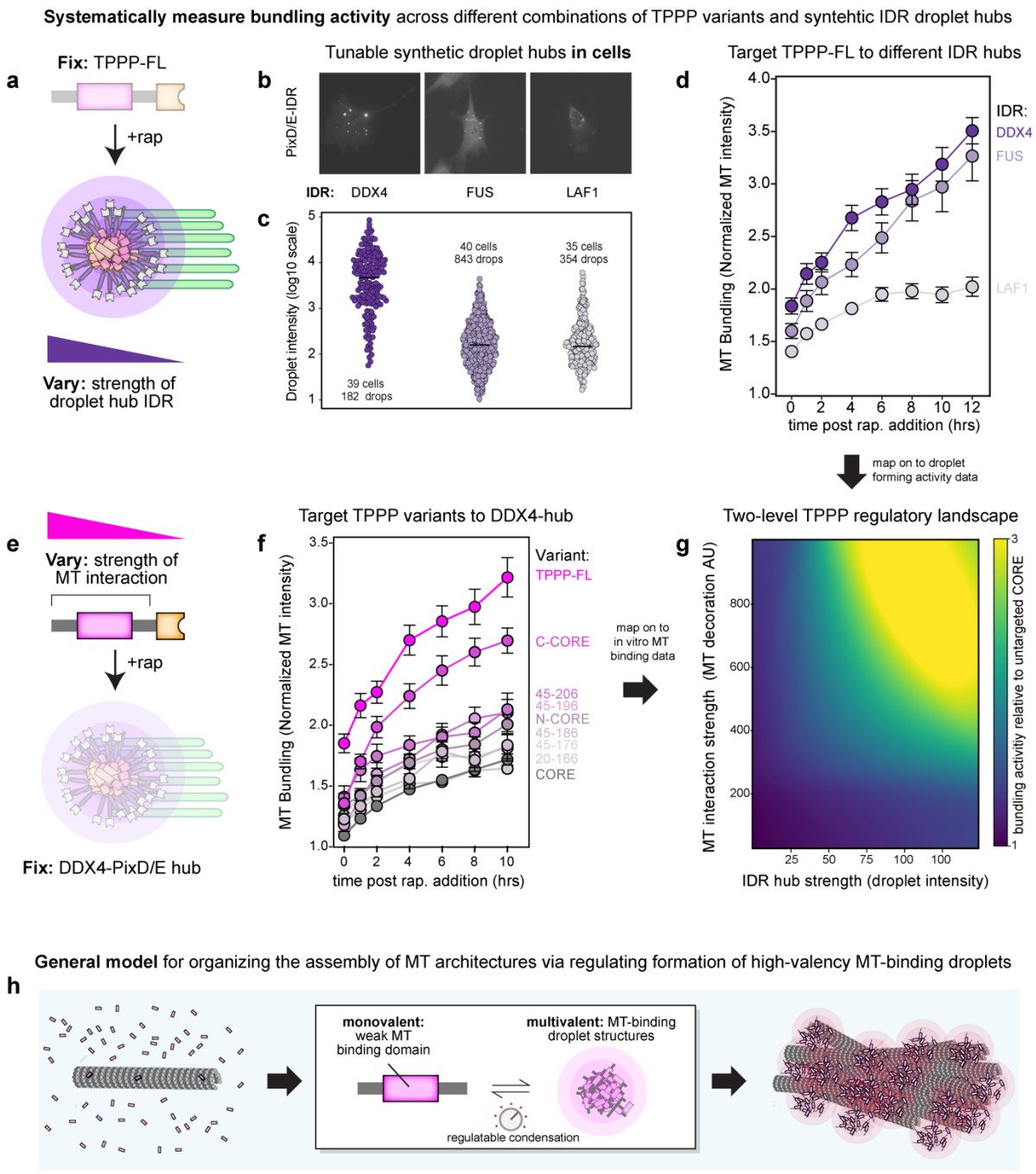

Fig. 5 | **Systematic targeting of TPPP variants to different synthetic droplet hubs suggests a two-level regulatory landscape for control of TPPP activity. a** Schematic depicting strategy for systematically targeting TPPP-FL to a panel of synthetic droplet hubs with different biophysical properties in cells by varying the IDR sequence used to promote droplet formation. **b** Representative images (FusionRed, white color in images) of droplet hubs in 3T3 cells derived from fusion of the indicated IDR (DDX4, FUS, and LAF-1) to FRB-PixD/E. Scale bar, 20 µm. **c** Quantification of FRB-IDRs-PixDE liquid droplets FusionRed fluorescence signal intensity in NIH3T3 cells. Medians are shown for 39, 40, and 35 representative cells were quantified, and the total numbers of the FRB-IDRs-PixDE droplets, respectively; FRB-DDX4-PixDE, n = 182; FRB-FUS-PixDE, n = 843; FRB-LAF-1-PixDE, n = 354. **d** The normalized intensity of SiR-tubulin signal near the cell center of cells co-transduced with FRB-IDRs-PixDE and TPPP FL-FKBP in NIH3T3 cells over 12 hrs following rapamycin treatment. Data are shown as (mean ± SEM, FRB-DDX4-PixDE/TPPP-FL-FKBP, n = 24; FRB-FUS-

PixDE/TPPP-FL-FKBP, n = 27; FRB-LAF-1-PixDE/TPPP-FL-FKBP, n = 31). **e** Schematic depicting strategy for systematically targeting TPPP variants with different MT interaction strengths to DDX4-droplet hubs. **f** The normalized intensity of SiR-tubulin signal near the cell center of cells co-transduced with FRB-DDX4-PixDE and TPPP variants-FKBP in NIH3T3 cells over 10 hrs following rapamycin treatment. Data are shown as (mean ± SEM, TPPP-FL-FKBP/FRB-DDX4-PixDE, n = 24; TPPPCcore-FKBP/FRB-DDX4-PixDE, n = 16; TPPPNcore-FKBP/FRB-DDX4-PixDE, n = 15; TPPP(45-206)-FKBP/FRB-DDX4-PixDE, n = 12; TPPP(45-196)-FKBP/FRB-DDX4-PixDE, n = 12; TPPP(45-186)-FKBP/FRB-DDX4-PixDE, n = 18; TPPP(45-176)-FKBP/FRB-DDX4-PixDE, n = 26; TPPP(20-166)-FKBP/FRB-DDX4-PixDE, n = 15; TPPP-CORE-FKBP/FRB-DDX4-PixDE, n = 36). **g** Bundling metrics were mapped to a TPPP variant's microtubule binding affinity (defined from single-MT binding assay) and the strength of the IDR hub (defined by a hub's frequency of large droplets) and interpolated to create a phenomenological phase portrait describing the observed two-level TPPP regulatory landscape from the experiments in a-f. **h** A general model for how TPPP and other MAPs can assemble higher-order MTs structure through combining a weak MT-binding domain with regulated condensation. Droplet formation creates high-valency structures that enhance binding, coating and bundling of microtubules.

References.

1. Haimo, L. T. & Rosenbaum, J. L. Cilia, flagella, and microtubules. *J. Cell Biol.* 91, 125s–130s (1981).

2. Vale, R. D. The Molecular Motor Toolbox for Intracellular Transport. *Cell* 112, 467–480 (2003).

3. Nogales, E. Structural insights into microtubule function. *Annu. Rev. Bioph. Biom.* 30, 397–420 (2001).

4. Olmsted, J. B. & Borisy, G. G. Microtubules. *Annu. Rev. Bioph. Biom.* 42, 507–540 (1973).

5. Goodson, H. V. & Jonasson, E. M. Microtubules and Microtubule-Associated Proteins. *Cold Spring Harb. Perspect. Biol.* 10, a022608 (2018).

6. Bodakuntla, S., Jijumon, A. S., Villablanca, C., Gonzalez-Billault, C. & Janke, C. Microtubule-Associated Proteins: Structuring the Cytoskeleton. *Trends Cell Biol.* 29, 804–819 (2019).

7. Chaaban, S. & Brouhard, G. J. A microtubule bestiary: structural diversity in tubulin polymers. *Mol. Biol. Cell* 28, 2924–2931 (2017).

8. LaFrance, B. J. *et al.* Structural transitions in the GTP cap visualized by cryo-electron microscopy of catalytically inactive microtubules. *Proc. Natl. Acad. Sci.* 119, e2114994119 (2022).

9. Saeidi, H. R., Lohrasebi, A. & Mahnam, K. External electric field effects on the mechanical properties of the αβ-tubulin dimer of microtubules: a molecular dynamics study. *J. Mol. Model.* 20, 2395 (2014).

10. Wang, B. *et al.* Liquid–liquid phase separation in human health and diseases. *Signal Transduct. Target Ther.* 6, 290 (2021).

11. Hyman, A. A., Weber, C. A. & Jülicher, F. Liquid-Liquid Phase Separation in Biology. *Annu. Rev. Cell Dev. Biol.* 30, 39–58 (2014).

12. Li, P. *et al.* Phase transitions in the assembly of multivalent signalling proteins. *Nature* 483, 336–340 (2012).

13. Brangwynne, C. P. *et al.* Germline P Granules Are Liquid Droplets That Localize by Controlled Dissolution/Condensation. *Science* 324, 1729–1732 (2009).

14. Chang, C.-C. & Hsia, K.-C. More than a zip code: global modulation of cellular function by nuclear localization signals. *FEBS J.* 288, 5569–5585 (2021).

15. Hernández-Vega, A. *et al.* Local Nucleation of Microtubule Bundles through Tubulin Concentration into a Condensed Tau Phase. *Cell Rep.* 20, 2304–2312 (2017).

16. King, M. R. & Petry, S. Phase separation of TPX2 enhances and spatially coordinates microtubule nucleation. *Nat. Commun.* 11, 270 (2020).

17. Sun, M. *et al.* NuMA regulates mitotic spindle assembly, structural dynamics and function via phase separation. *Nat. Commun.* 12, 7157 (2021).

18. Song, X. *et al.* Phase separation of EB1 guides microtubule plus-end dynamics. *Nat. Cell Biol.* 25, 79–91 (2023).

19. Maan, R. *et al.* Multivalent interactions facilitate motor-dependent protein accumulation at growing microtubule plus-ends. *Nat. Cell Biol.* 25, 68–78 (2023).

20. Mah, D. *et al.* The Sulfation Code of Tauopathies: Heparan Sulfate Proteoglycans in the Prion Like Spread of Tau Pathology. *Front. Mol. Biosci.* 8, 671458 (2021).

21. Alfaro-Aco, R., Thawani, A. & Petry, S. Structural analysis of the role of TPX2 in branching microtubule nucleation. *J. Cell Biol.* 216, 983–997 (2017).

22. Chang, C.-C., Huang, T.-L., Shimamoto, Y., Tsai, S.-Y. & Hsia, K.-C. Regulation of mitotic spindle assembly factor NuMA by Importin-β. *J. Cell Biol.* 216, 3453–3462 (2017).

23. Kanaan, N. M., Hamel, C., Grabinski, T. & Combs, B. Liquid-liquid phase separation induces pathogenic tau conformations in vitro. *Nat. Commun.* 11, 2809 (2020).

24. Meier, S. M. *et al.* Multivalency ensures persistence of a +TIP body at specialized microtubule ends. *Nat. Cell Biol.* 25, 56–67 (2023).

25. Maan, R. *et al.* Multivalent interactions facilitate motor-dependent protein accumulation at growing microtubule plus-ends. *Nat. Cell Biol.* 25, 68–78 (2023).

26. Vincze, O. *et al.* Tubulin Polymerization Promoting Proteins (TPPPs): Members of a New Family with Distinct Structures and Functions. *Biochemistry* 45, 13818–13826 (2006).

27. DeBonis, S., Neumann, E. & Skoufias, D. A. Self protein-protein interactions are involved in TPPP/p25 mediated microtubule bundling. *Sci. Rep.* 5, 13242 (2015).

28. Fu, M. *et al.* The Golgi Outpost Protein TPPP Nucleates Microtubules and Is Critical for Myelination. *Cell* 179, 132-146.e14 (2019).

29. Heng, Y.-W. *et al.* TPPP acts downstream of RhoA–ROCK–LIMK2 to regulate astral microtubule organization and spindle orientation. *J. Cell Sci.* 125, 1579–1590 (2012).

30. Oláh, J. & Ovádi, J. Pharmacological targeting of α-synuclein and TPPP/p25 in Parkinson's disease: challenges and opportunities in a Nutshell. *FEBS Lett.* 593, 1641–1653 (2019).

31. Oláh, J., Bertrand, P. & Ovádi, J. Role of the microtubule-associated TPPP/p25 in Parkinson's and related diseases and its therapeutic potential. *Expert Rev. Proteomic* 14, 301–309 (2017).

32. Ubhi, K., Low, P. & Masliah, E. Multiple system atrophy: a clinical and neuropathological perspective. *Trends Neurosci.* 34, 581–590 (2011).

33. Patel, A. *et al.* A Liquid-to-Solid Phase Transition of the ALS Protein FUS Accelerated by Disease Mutation. *Cell* 162, 1066–1077 (2015).

34. McGurk, L. *et al.* Poly(ADP-Ribose) Prevents Pathological Phase Separation of TDP-43 by Promoting Liquid Demixing and Stress Granule Localization. *Mol. Cell* 71, 703-717.e9 (2018).

35. Elbaum-Garfinkle, S. *et al.* The disordered P granule protein LAF-1 drives phase separation into droplets with tunable viscosity and dynamics. *Proc. Natl. Acad. Sci.* 112, 7189–7194 (2015).

36. Nott, T. J. *et al.* Phase Transition of a Disordered Nuage Protein Generates Environmentally Responsive Membraneless Organelles. *Mol. Cell* 57, 936–947 (2015).

37. André, A. A. M. & Spruijt, E. Liquid–Liquid Phase Separation in Crowded Environments. *Int. J. Mol. Sci.* 21, 5908 (2020).

38. Lin, Y., Currie, S. L. & Rosen, M. K. Intrinsically disordered sequences enable modulation of protein phase separation through distributed tyrosine motifs. *J. Biol. Chem.* 292, 19110–19120 (2017).

39. Zhang, X. *et al.* The proline-rich domain promotes Tau liquid–liquid phase separation in cells. *J. Cell Biol.* 219, e202006054 (2020).

40. Shin, Y. *et al.* Spatiotemporal Control of Intracellular Phase Transitions Using Light-Activated optoDroplets. *Cell* 168, 159-171.e14 (2017).

41. Ori-McKenney, K. M., Jan, L. Y. & Jan, Y.-N. Golgi Outposts Shape Dendrite Morphology by Functioning as Sites of Acentrosomal Microtubule Nucleation in Neurons. *Neuron* 76, 921–930 (2012).

42. Valenzuela, A., Meservey, L., Nguyen, H. & Fu, M. Golgi Outposts Nucleate Microtubules in Cells with Specialized Shapes. *Trends Cell Biol.* 30, 792–804 (2020).

43. Chung, C. G. *et al.* Golgi Outpost Synthesis Impaired by Toxic Polyglutamine Proteins Contributes to Dendritic Pathology in Neurons. *Cell Rep.* 20, 356–369 (2017).

44. Rebane, A. A. *et al.* Liquid–liquid phase separation of the Golgi matrix protein GM130. *FEBS Lett.* 594, 1132–1144 (2020).

45. Chang, C.-C. *et al.* Ran pathway-independent regulation of mitotic Golgi disassembly by Importin-α. *Nat. Commun.* 10, 4307 (2019).

46. Ren, S., Sato, R., Hasegawa, K., Ohta, H. & Masuda, S. A Predicted Structure for the PixD–PixE Complex Determined by Homology Modeling, Docking Simulations, and a Mutagenesis Study. *Biochemistry* 52, 1272–1279 (2013).

47. Yuan, H. & Bauer, C. E. PixE promotes dark oligomerization of the BLUF photoreceptor PixD. *Proc. Natl. Acad. Sci.* 105, 11715–11719 (2008).

48. Dine, E., Gil, A. A., Uribe, G., Brangwynne, C. P. & Toettcher, J. E. Protein Phase Separation Provides Long-Term Memory of Transient Spatial Stimuli. *Cell Syst.* 6, 655-663.e5 (2018).

49. Lehotzky, A. *et al.* Dynamic targeting of microtubules by TPPP/p25 affects cell survival. *J. Cell Sci.* 117, 6249–6259 (2004).

50. Efimov, A. *et al.* Asymmetric CLASP-Dependent Nucleation of Noncentrosomal Microtubules at the trans-Golgi Network. *Dev. Cell* 12, 917–930 (2007).

51. Hong, S. K., Kim, K.-H., Song, E. J. & Kim, E. E. Structural Basis for the Interaction between the IUS-SPRY Domain of RanBPM and DDX-4 in Germ Cell Development. *J. Mol. Biol.* 428, 4330–4344 (2016).

52. Castrillon, D. H., Quade, B. J., Wang, T. Y., Quigley, C. & Crum, C. P. The human VASA gene is specifically expressed in the germ cell lineage. *Proc. Natl. Acad. Sci.* 97, 9585–9590 (2000).

53. Zhu, F. *et al.* Deficiency of TPPP2, a factor linked to oligoasthenozoospermia, causes subfertility in male mice. *J. Cell Mol. Med.* 23, 2583–2594 (2019).

54. Orosz, F. & Ovádi, J. TPPP orthologs are ciliary proteins. *FEBS Lett.* 582, 3757–3764 (2008).

55. Gouveia, B. *et al.* Capillary forces generated by biomolecular condensates. *Nature* 609, 255–264 (2022).

56. Teixidó-Travesa, N., Roig, J. & Lüders, J. The where, when and how of microtubule nucleation – one ring to rule them all. *J. Cell Sci.* 125, 4445–4456 (2012).

57. Bornens, M. The Centrosome in Cells and Organisms. *Science* 335, 422–426 (2012).

58. Rios, R. M. The centrosome–Golgi apparatus nexus. *Philos. Trans. R. Soc.* 369, 20130462 (2014).

59. Park, H. *et al.* Optogenetic protein clustering through fluorescent protein tagging and extension of CRY2. *Nat. Commun.* 8, 30 (2017).